Journal of Materials Chemistry A

Investigation of MgO additives on microstructure and properties of thin LLZO electrolytes for all-solid-state batteries

Journal:	*Journal of Materials Chemistry A*
Manuscript ID	TA-ART-12-2024-009002.R1
Article Type:	Paper
Date Submitted by the Author:	04-Feb-2025
Complete List of Authors:	Go, Wooseok; Lawrence Berkeley National Laboratory, Doeff, Marca; Lawrence Berkeley National Laboratory, Tucker, Michael; Lawrence Berkeley National Laboratory

Investigation of MgO additives on microstructure and properties of thin LLZO electrolytes for all-solid-state batteries

Wooseok Go, Marca M. Doeff, Michael C. Tucker*

Energy Storage and Distributed Resources Division, Lawrence Berkeley National Laboratory, Berkeley, CA 94720

*Corresponding author: mctucker@lbl.gov

Abstract

To realize high-energy density lithium lanthanum zirconate (LLZO)-based solid-state batteries (SSB), LLZO electrolytes should be fabricated with low thickness and high mechanical strength. An effective strategy for strengthening ceramic materials is to use additives. Here, we employed MgO nanopowders and fibers as additives for the thin LLZO electrolyte in order to improve the mechanical strength. The microstructure, mechanical properties, and electrochemical properties are characterized to investigate the effects of adding MgO and sintering time. The MgO remains at grain boundaries after sintering, making the microstructure of LLZO fine and uniform. The mechanical strength of the MgO-added LLZO was enhanced by more than 60 % while maintaining high ionic conductivity ($1x10^{-4}$ S/cm) at room temperature. Li symmetric cells using the MgO fiber-LLZO and MgO powder-LLZO exhibit 2 and 3 times higher critical current density (CCD) than those of pure LLZO, and a solid-state full cell exhibits stable cycling performance. These results demonstrate that the use of MgO nanopowder or fiber as an additive for thin LLZO is beneficial for high-current density cycling, by improving mechanical properties and microstructure.

Keywords: LLZO electrolyte; mechanical strength; microstructure; solid state battery; additives

Introduction

All-solid-state batteries (ASSB) are a promising replacement for conventional organic liquid-based Li-ion batteries owing to their potential for higher energy density and improved safety. The solid electrolyte is a crucial component of ASSBs, and several options exist including sulfides, halides, and oxides. Among the oxide materials, Lithium Lanthanum Zirconium Oxide (LLZO) has been gaining attention as a prominent solid electrolyte material due to its high ionic conductivity (>$1x10^{-4}$ S/cm at room temperature) and apparent stability versus lithium metal.[1] To maximize the energy density in LLZO-based ASSBs, the LLZO electrolyte must be very thin (≤20 μm).[2, 3] In a previous study,[4] tape-casting was used to fabricate thin LLZO electrolytes. To optimize this tape-casting process, binders and additives were explored, and 40~250 μm thicknesses of LLZO were successfully fabricated.[4, 5] Despite such success in fabricating thin LLZO, challenges in mechanical properties persist. As the thickness is reduced, the LLZO becomes too fragile to handle due to its brittle nature.[6] For example, 20 μm thickness LLZO breaks under a very light loading (36.5 mN).[7] Thus, to realize a thin LLZO electrolyte, the mechanical strength should be improved.

For classic structural ceramics (e.g., Al_2O_3 and ZrO_2), increasing mechanical strength has been intensively explored.[8, 9] The ceramic strengthening strategies include reducing defects (pores, internal cracks) using advanced fabrication techniques, making grain size small and uniform, introducing additive particles and/or bridging pillars in the ceramic body, surface glazing, and chemical etching.[10-12] Some of these strategies were adopted to ceramic solid electrolyte materials and successfully improved their mechanical strength. For example, the fracture strength of Na-β”-alumina was increased by incorporating zirconia particles due to a phase transformation

toughening effect.[13-15] Fracture toughness of LATP was increased by introducing reduced graphene oxide as a bridging pillar.[16] The fracture strength of LLZO was improved by using high-pressure assisted fabrication processes and introducing additive particles.[17-19] Oscillatory pressure sintering increased the fracture strength by ~48 % due to reduced defect sizes (i.e., pores) .[17] Introducing MgO particles into Ta-doped LLZO increased fracture strength from 105 to 145 MPa owing to reduced grain size and less abnormal grain growth (AGG).[18] The strength was further improved to 160 MPa after optimizing the sintering protocol.[19] However, the high-pressure assisted techniques have technical difficulties for scaling up to large area fabrication, and the MgO additive studies were conducted only with thick (~1 mm) LLZO electrolytes and cell cycling was not conducted.

In our previous study, MgO nano-particles were used as an additive for thin LLZO.[4] MgO contents, binder and solvent selections, sintering conditions, and electrochemical properties were studied, and we successfully fabricated ~100 μm thickness LLZO with 2.2×10^{-4} S/cm conductivity. However, the mechanical properties and electrochemical performance in symmetric and full cells were not studied. Only simple MgO particles have been studied as an additive for LLZO, not alternative structures such as fibers. In this study, MgO nanoparticles or fibers were incorporated into thin (~80 μm) LLZO electrolytes and sintered for different lengths of time, and the effect on microstructure, properties, and electrochemical performance in symmetric and full cells was investigated. Microstructure observation shows that the MgO is present at the LLZO grain boundary, and the MgO reduces the size of LLZO grains and makes the microstructure uniform. Due to the change in the microstructure, the MgO-added LLZO exhibits >60 % increased mechanical strength, with minimal impact on conductivity. Li symmetric cells using the MgO-LLZO also show a threefold increase in critical current density (CCD) when cycled at 25 ℃, with

no added pressure, in an all-solid state configuration. Furthermore, full cells with the MgO powder-LLZO electrolytes were fabricated and demonstrated successful cycling at 25 ℃. In addition to the improvement to the mechanical properties and CCD, an additional advantage to this approach is its scalability.

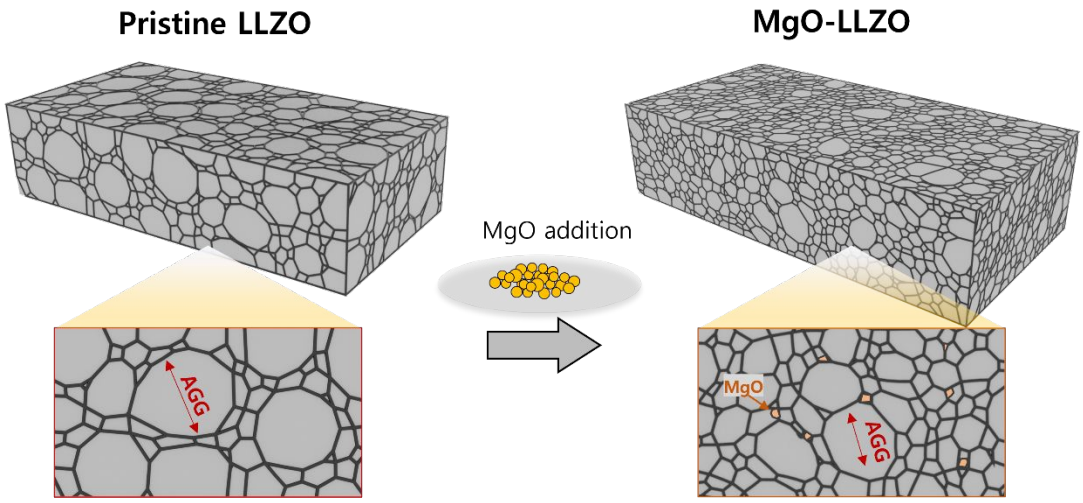

Figure 1. Schematic illustration of MgO in the microstructure of LLZO electrolyte.

Experimental

LLZO fabrication

A tape casting process was used for preparing thin LLZO electrolytes. Al-substituted LLZO powder ($Li_{6.25}Al_{0.25}La_3Zr_2O_{12}$, 500 nm, MSE Supplies), Li_2CO_3 (5 wt%, Sigma-Aldrich >99.0 %), dispersant (DS002, Polymer Innovations), and MgO powder (5 wt%, 50 nm, US Research Nanomaterials Inc.) or MgO fiber (5 wt%, Bonding Chemical) were mixed in toluene. LLZO without MgO was also prepared for comparison. The mixed slurry was ball milled for 30 min at 500 rpm using ZrO_2 balls (3 mm diameter) and a planetary ball milling machine (PM200, Retsch).

Subsequently, a binder (MSB-1-13, Polymer Innovations) was added and mixed for 3 hours at 50 rpm using a roller jar mill (Thermoscientific). Using the mixed slurry, tape casting was conducted on a carrier film (Si-coated polyethylene terephthalate (PET) film). A tape casting coater (MSK-AFA-I, MTI) and doctor blade (gap: 200 μm) were used for the tape casting. The casted films were dried overnight under an ambient air atmosphere. The dried films were detached from the substrate and cut into appropriate sizes. The films were stacked and placed between two Si-PET films, then laminated using a hot-pressing machine (4389, Carver). The lamination was conducted at a temperature of 90 ℃ and pressure of 20 MPa for 10 minutes. The laminated films were heated under an air atmosphere at 710 ℃ for 16 hours in a box furnace (Thermolyne, Thermo Scientific) to fully burn out the binder. For sintering, an Al_2O_3 block was used as a substrate, and the LLZO films were placed between two carbon papers (Pyrolytic Graphite Sheet, Panasonic). A thin Al_2O_3 plate was placed on the samples to prevent curving during sintering. Sintering was conducted for various times in a tube furnace (OTF-1200X, MTI) under Ar flowing atmosphere (200 mL/min) at 1050 ℃. The digital photo of the sintered LLZO and MgO-LLZO is shown in Figure S1.

Characterization

The microstructures were observed using scanning electron microscopy (SEM, JSM-7500F, JEOL) with an accelerating voltage of 10 keV. The grain size was analyzed using the ImageJ program. The distribution of MgO particles was observed using Energy-dispersive X-ray spectroscopy (EDS, Quanta FEG-250, FEI). The ionic conductivity was measured using electrochemical impedance spectroscopy (EIS, Bio-Logic VSP-300) over a frequency range of 0.1 Hz to 7 MHz. For the EIS, gold blocking electrodes were deposited on both sides of the LLZO using a sputtering machine (108 Auto, Cressington sputter). X-ray diffraction (XRD, D2 Phaser,

Bruker) patterns were collected to identify the crystal phase of the sintered LLZO. Fracture strengths were measured using a Dynamic Mechanical Analysis machine (DMA, Q800, TA Instruments). A small size 3-point bending fixture was used for the fracturing test. Specimen dimensions were 10 mm length, 5.4 mm wide, and thickness 0.08 mm. For each type of sample, 3 point bending tests were conducted with more than three specimens.

Symmetric cell fabrication

Au was sputtered on both sides of LLZO (sintered at 1050 ℃ for 4 hours). Li metal was cut into a proper size and attached to the Au sputtered surface, then the Li was heated at 250 ℃ in an Ar-filled glove box. The Li melted and wet onto the Au-coated surface. Coin cell cases (2032, MTI) with crimpers were used for cell assembly. Instead of a conventional metallic spring, a soft carbon felt was used to prevent the fracture of thin LLZO, while maintaining electronic conduction. The assembled symmetric cells were cycled using a potentiostat (Bio-Logic, VMP-300) in a temperature-controlled chamber at 25 ℃. For CCD tests, current densities of 10 to 1000 $\mu A/cm^2$ were used, and the cells were charged and discharged for 1 hour each, with increasing current density applied every 5 cycles.

Solid-state full-cell fabrication

Full cell assembly was carried out in an Ar-filled glove box. A MgO powder-LLZO film (sintered at 1050 ℃ for 4 hours) was used as a solid electrolyte. The Li metal anode was prepared on one side of the MgO-LLZO using the same method as described above. The cathode active material (CAM) was $LiNbO_3$ (1 wt%) coated NMC 811 ($LiNi_{0.8}Mn_{0.1}Co_{0.1}O_2$, Ampcera), the conducting material was carbon black (Acetylene black, DENKA), and the solid-catholyte was dual salt-

succinonitrile mixture (LiTFSI-LiBOB-SN, LiTFSI:LiBOB:SN in a mole ratio of 3:2:95).[20] As a cathode current collector, carbon paper was used. At 80 ℃, the CAM, carbon black, and the molten catholyte were mixed at a weight ratio of 19.6:2.4:78.0. The mixed slurry was spread onto the carbon paper (active material loading: 2.4 mg/cm^2), then placed on the MgO-LLZO side on which gold was not sputtered. This step also formed intimate interfacial contact between the electrode and LLZO. The stacked cell components were cooled down to room temperature (solidifying the catholyte) in coin cell cases, and the cell case was then sealed. The full cells were cycled using a potentiostat (Arbin, LBT21084) at 0.1 C-rate, without any exogenous pressure, at 25 ℃ in a temperature-controlled chamber.

Results and Discussion

Phase and microstructure characterization

XRD patterns of MgO-powder-added LLZO (MgO-LLZO) sintered for two different lengths of time (2 hours in red, 10 hours in black) at 1050 ℃ were collected and are shown in Figure 2a. The XRD patterns match well with the reference cubic LLZO pattern (ICSD 98-042-2259), which is the desired phase. XRD peaks corresponding to MgO were not observed because the MgO content was small (~5 wt%) and Mg is light, and the LLZO peak intensities were relatively strong. For the MgO-LLZO after 10 hours of sintering, an additional peak at $2\theta = 28.5^{o}$ was observed. This peak corresponds to $La_2Zr_2O_7$, which results from Li evaporative loss during a long sintering time.[4, 21] The same trend in XRD patterns was observed with LLZO (Figure S2). In order to observe the location of the MgO in the LLZO film before and after the sintering, SEM / EDS elemental mapping was conducted (Figure 2b-e, Figure S3). Before sintering, MgO particles were evenly

distributed between the nano-sized LLZO particles throughout the raw film (Figure 2b-c). After sintering, micro-size LLZO grains (light grey color in Figure 2d) were observed, and the MgO particles (dark grey color) are observed at the grain boundaries. The EDS mapping image (Figure 2e, red is Mg and cyan is Zr) confirms that the small particles are MgO, and their particle size remains similar after sintering. These XRD and SEM observations show that the MgO doesn't react with the LLZO phase, instead, it remains at the grain boundary. The presence of MgO at the grain boundary can be attributed to the low chemical reactivity and high melting temperature (>1400 ℃) of MgO.[22]

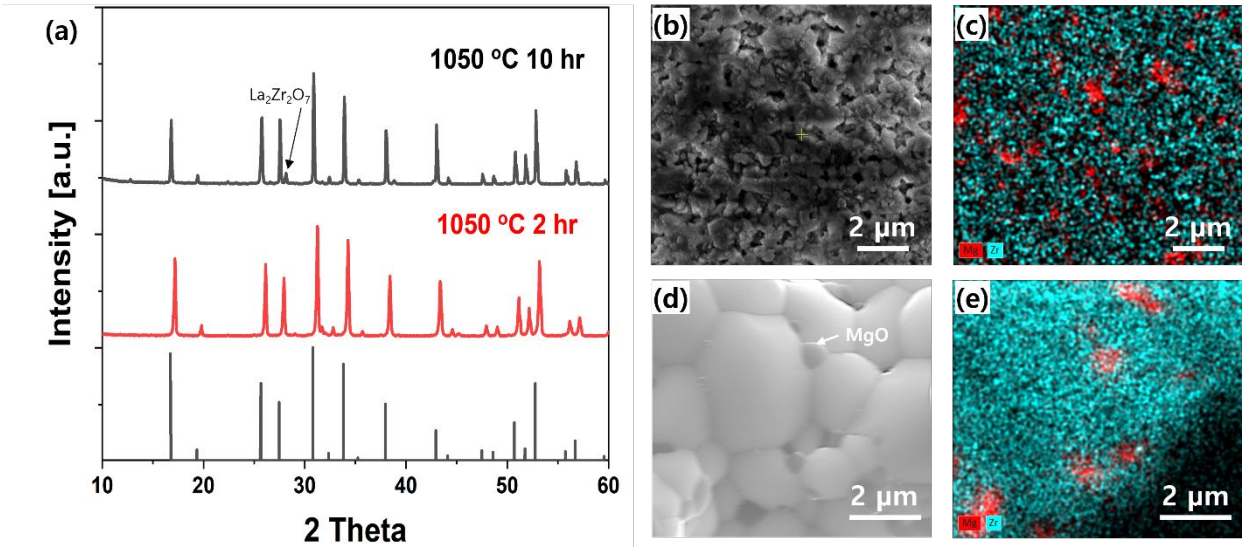

Figure 2. Phase and microstructure of the sintered MgO-LLZO electrolyte. (a) XRD patterns of the MgO-LLZO sintered for different lengths of time, as indicated. (b,d) Surface SEM image and (c,e) EDS mapping image of the (b,c) raw LLZO film and (d,e) sintered LLZO film.

To investigate the effect of MgO on the microstructure of LLZO, SEM was used. Figure 3a-b shows surface SEM images of LLZO, processed without MgO, after 2 and 10 hours of sintering. Both of them exhibited a highly dense microstructure (density of ~95 %, Figure S4), but the

difference in grain size is noticeable. The grain size distribution is plotted in Figure 3c. The distribution shows that the average grain size increased from 1.3 to 4.9 μm after increasing the sintering time from 2 hours to 10 hours and shows a multimodal distribution. Grain growth with a longer sintering time is a typical behavior of ceramic materials. For the 2 hour-LLZO, the major peak was at 0.98 μm and a minor peak was at 3.86 μm. The relatively large grains (as also observed in the SEM images, Figure 3a-b) are the result of abnormal grain growth (AGG), which indicates a few grains grow much larger than the rest of the grains in ceramics. AGG in LLZO (grain size 100~200 μm[20-22]) was also observed in previous studies and led to loose grain boundaries, lower density, lower strength, and reduced CCD.[18, 23-25] Similarly, 10 hour-LLZO exhibited increased amounts of AGG (5 % for 2 hour-LLZO, 15 % for 10 hour-LLZO) with the distinctive shape of AGG grains clearly visible (Figure 3b).

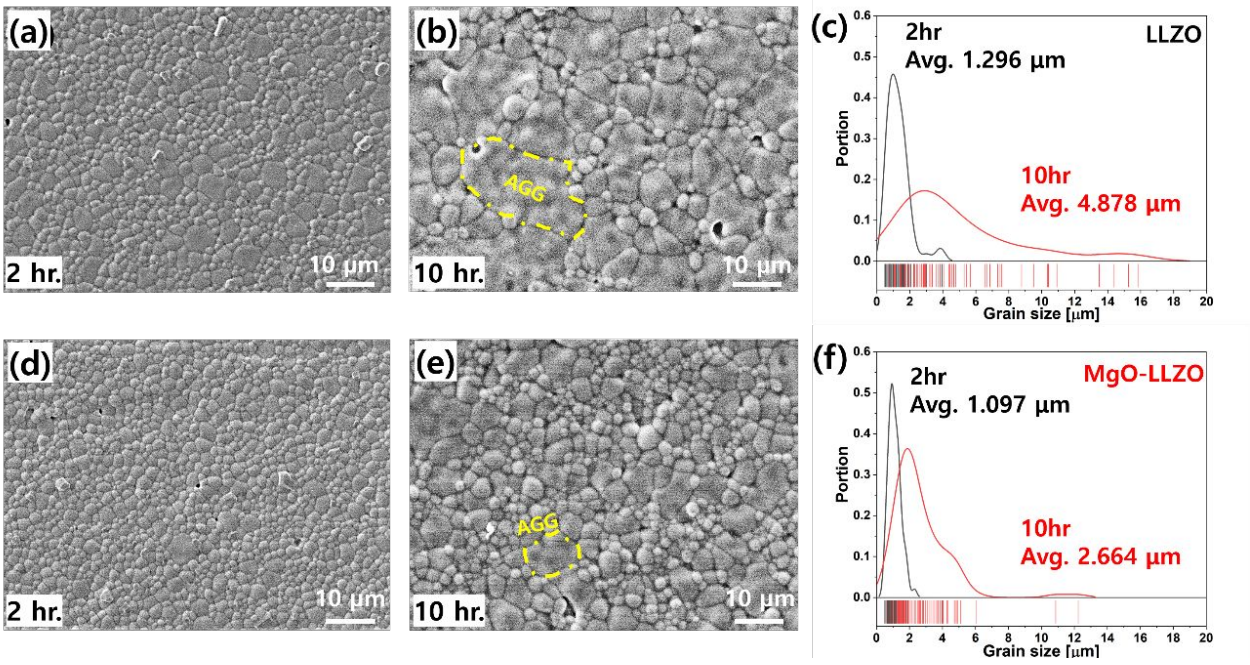

Figure 3. Grain size observation on LLZO and MgO-LLZO. Surface SEM image of as-sintered external surface of LLZO after (a,d) 2 hours and (b,e) 10 hours of sintering at 1050°C, and (c,f) grain size distribution of (a-c) LLZO and (d-f) MgO-LLZO.

The microstructure of the MgO-LLZO is shown in Figure 3d-f. The MgO-LLZO also exhibited a high density (~95 %) as shown in Figure S4. It is clear that the grain size of MgO-LLZO is finer compared to the LLZO processed without MgO. The average grain size was 15.4 % smaller (1.1 μm) for the 2 hours sample and 45.4 % smaller (2.7 μm) for the 10 hours sample compared to that of LLZO sintered without MgO. The grain size distributions (Figure 3f) of the MgO-LLZO also exhibit multimodal distributions but with much narrower ranges. For the samples sintered for 2 hours, the major peak was at 0.96 μm, and the minor peak at 2.35 μm. The gap between the two peaks was 1.39 μm which is narrower than that of the LLZO without MgO (2.88 μm). For the 10 hours samples, the difference in grain size distribution between LLZO (Figure 3c, red) and MgO-LLZO (Figure 3f, red) became more distinctive. These results imply that adding MgO reduces the grain growth rate and retards AGG, resulting in LLZO having a finer and more uniform microstructure. The reduced grain growth rate and homogenized microstructure by adding MgO is consistent with previous reports in Al_2O_3 ceramics [26-29] and LLZO electrolytes. [30, 31]

In addition to the fine MgO powder discussed above, LLZO was also processed with MgO fibers (MgO fiber-LLZO), and the microstructures are presented in Figure S5. The as-received MgO fibers were ~ 10-25 μm long and ~1-5.3 μm. After sintering for 4 hours at 1050 ℃, the MgO fibers maintained their shape and attached to LLZO grains as shown in Figure S5b-d. The size of LLZO grains was about 1~2 μm (Figure S5c) and no abnormal grain growth was observed.

Mechanical and electrochemical property characterization

Mechanical properties of the LLZO and MgO-LLZO samples sintered for different lengths of time were compared using 3-point bending tests as shown in Figure 4a. For LLZO after 2 hours of sintering, the fracture strength was ~153 MPa. This strength is in the middle of the typical strength range (100~250 MPa) reported for LLZO in previous studies.[6, 17, 18, 32] When the sintering time was extended to 10 hours, the fracture strength decreased to ~103 MPa, which is close to the lower limit of the range. This reduction can be attributed to the differences in micro-structure rather than density because the densities of all samples were around 95% (Figure S4). It is generally recognized that increases in grain size and AGG make ceramics mechanically weak. Knudsen *et al.*[33] suggested a general relationship between microstructure and mechanical strength with equation 1,

$$S = kG^{-a}e^{-bP} \quad (1)$$

where S is mechanical strength, G is grain size, P is porosity, e is Euler's constant, and k, a, and b are positive constants. The equation implies that strength is inversely proportional to grain size and agrees with our observation in Figure 4(a).

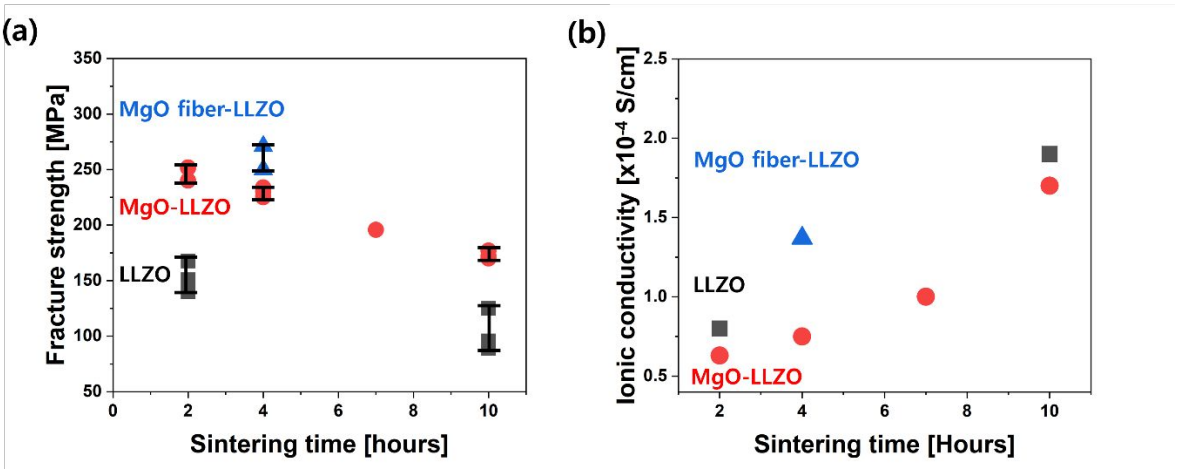

Figure 4. Mechanical and conductivity characterization. (a) Fracture strength and (b) ionic conductivities of LLZO (gray), MgO-LLZO (red), and MgO-fiber-LLZO (blue) as a function of sintering time.

The MgO-LLZO showed a similar relationship between the sintering time and fracture strength. After 2 hours, the strength was 248 MPa which is at the upper end of the typical strength range (100-250 MPa) and significantly higher than that of the sample processed without MgO. The strength is particularly notable because of the low thickness (~80 μm, Figure S6). When the sintering time was extended (up to 10 hours), the strength was reduced to 173 MPa. This can also be attributed to the increased grain size and AGG at the longer sintering time. It is notable that the MgO-LLZO still showed >60 % increased strength compared to LLZO processed without MgO when the sintering time was extended. This significant improvement is also attributed to the difference in microstructure rather than density because both types (MgO and no-MgO LLZO) had similar densities of ~95 % after 2 hours (Figure S4). As presented in Figure 3, the MgO-LLZO also exhibited a mechanically favorable microstructure including smaller grain sizes and less AGG. These results show that adding MgO makes the LLZO mechanically strong due to its smaller grain size and uniform microstructure.

The mechanical properties of MgO fiber processed LLZO are also shown in Figure 4a. The strength of the MgO fiber-LLZO was 261 MPa, which is 13 % higher than that of the MgO-LLZO sintered for the same length of time (4 hours). This enhancement in strength can be attributed to a fiber toughening effect which increases the toughness of ceramic by incorporating high-modulus fibers (or whiskers) into the ceramic body, [11, 34] since the MgO fiber has a higher Young's modulus (~300 GPa)[35] than LLZO (~150 GPa)[36].

Ionic conductivities of the different LLZO samples after sintering at various times were measured using EIS (Figure S7) and are shown in Figure 4(b). The conductivity increased with sintering time for both sets of samples and the MgO-LLZO conductivities were slightly lower than for LLZO processed without MgO. For the MgO fiber-LLZO, it has a higher conductivity than the MgO-LLZO and LLZO sintered for the same length of time. Because all the specimens for the ionic conductivity measurement have similar densities, the differences and trend in ionic conductivities are related to microstructure. When the grain size is smaller (e.g., for short sintering times and/or MgO added), the ionic conductivity is reduced. On the other hand, when the grain size increased (e.g., for long sintering times and/or no added MgO), conductivity increased. This trend may be attributed to the lower ionic conductivity of grain boundaries compared to grains in LLZO.[37] For the smaller grain size LLZO, there are more grain boundaries that inhibit facile Li-ion conduction, resulting in reduced total ionic conductivity. These results indicate that adding MgO powder is not beneficial for ionic conductivity because it reduces grain size, however the impact is small relative to the large improvement in mechanical properties. It is also noteworthy that compromised ionic conductivity of MgO-LLZO can be overcome by further optimization as shown in Figure S8. When LLZO was processed with lower additive content (3 % Li_2CO_3 and 2 % MgO) and sintered at a higher temperature (1080 ℃), the conductivity was $3.3x10^{-4}$ S/cm (Figure S8b), which is on the higher limit of ionic conductivities reported for Al-substituted LLZO.

Electrochemical performance

Critical current densities (CCD) were determined using Li/LLZO/Li symmetric cells with LLZO, MgO fiber-LLZO, and MgO-LLZO. The inset schematic in Figure 5a shows the symmetric cell configuration. The symmetric cells cycling was conducted under 25 ℃ and without any exogenous

pressure. For LLZO processed without MgO (Figure 5a), the symmetric cell exhibited a stable voltage profile up to 50 μA/cm^2. When the current density was increased from 10 to 50 μA/cm^2, the overpotential increased from 2.3 to 10.7 mV. At a current density of 100 μA/cm^2, the voltage sharply dropped indicating that there was a short-circuit induced by dendrite growth. Therefore, the CCD of the LLZO was determined to be 100 μA/cm^2 (100 μAh/cm^2). This CCD value is the same as was reported in our previous study for a similar cell.[6] For the cell containing the MgO fiber-LLZO (Figure 5b), there was a stable voltage response up to 100 μA/cm^2 (overpotential 20.8 mV) but some voltage instability was observed when the current density was increased to 200 μA/cm^2. Thus, the CCD of the cell containing MgO fiber-LLZO is approximately twice that of the one containing unmodified LLZO (200 μA/cm^2 or 200 μAh/cm^2). The symmetric cell containing MgO-LLZO (Figure 5c) also showed a similar voltage response and overpotential up to 50 μA/cm^2 as the other cells, due to the similar ionic conductivities (~1x10^{-4} S/cm). At current densities higher than that, MgO-LLZO maintained a stable voltage profile up to 300 μA/cm^2 (300 μAh/cm^2), corresponding to 3 times higher CCD than LLZO. The improvement of CCD upon MgO addition was further confirmed with another batch of LLZO powder with different additive loadings and sintering conditions (Figure S9). Under a high areal capacity (1 mAh/cm^2) cycling condition, the MgO-LLZO still showed 3 times higher CCD (300 μA/cm^2) compared to that of the pure LLZO (100 μA/cm^2). These values are among the highest reported for thin samples of LLZO (Table S1, Figure S10) and are notable due to the demanding cycling conditions (25 ℃, no added pressure, no liquid, high areal capacity, 5 cycles). The improvement can be attributed to the higher mechanical strength of the MgO-modified materials, which can inhibit Li dendrite growth. Improvement in CCD correlated with improved mechanical strength has also been reported in other studies.[31]

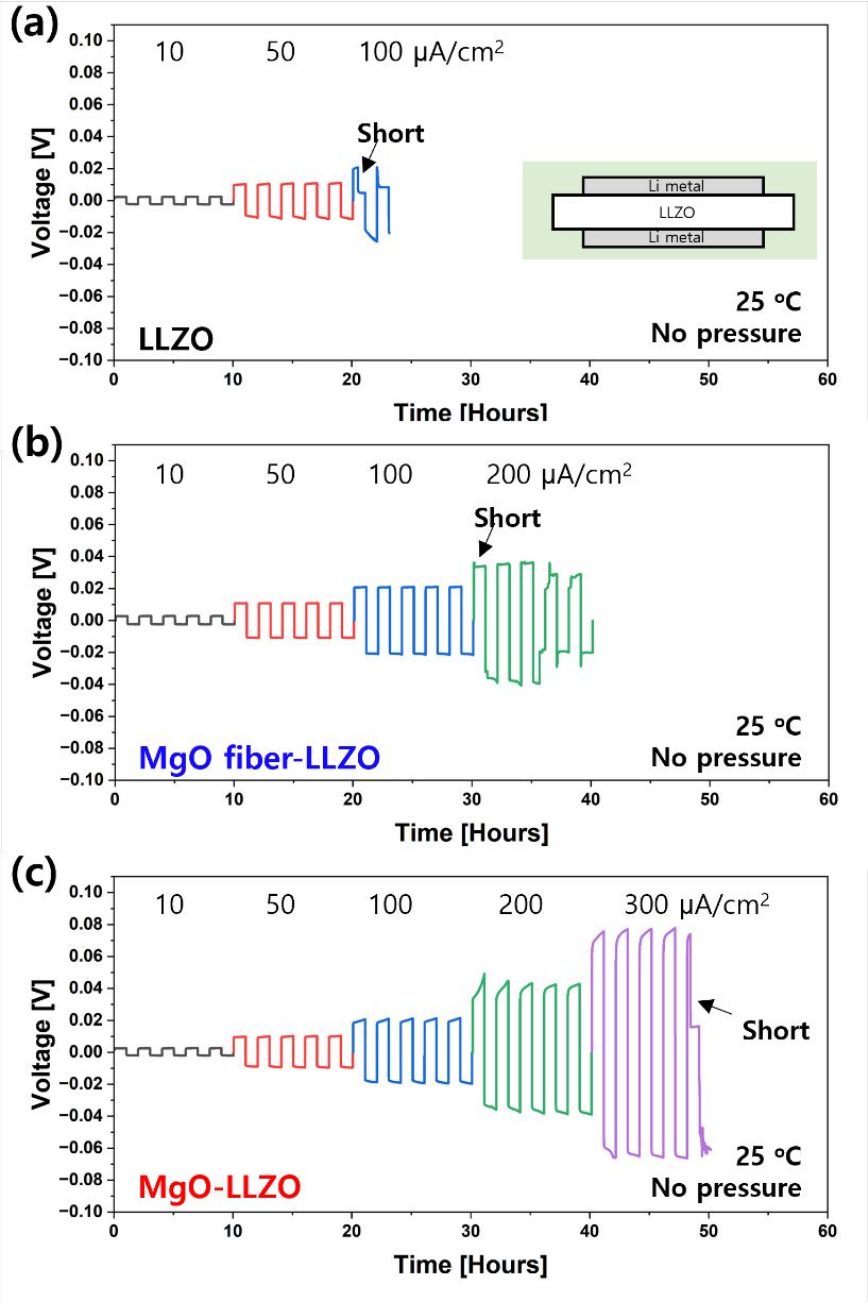

Figure 5. Critical current density test using Li symmetric cells. Voltage profile of the symmetric cell cycling using (a) LLZO, (b) MgO fiber-LLZO, and (c) MgO-LLZO. The symmetric cells were cycled at 25 ℃and no pressure applied condition.

Additionally, solid-state full cells were fabricated using the MgO-LLZO and tested as shown in Figure 6. The thickness of MgO-LLZO was 80 μm. Although mechanical strength of LLZO was improved by MgO, below 80 μm it was difficult to reliably handle and assemble into coin cells, and some samples cracked. $LiNbO_3$ coated-NMC811 (expected practical capacity ~180 mAh/g) was used as a cathode active material (CAM), and Li metal as an anode. The full cell was cycled at 25 ℃ and without any exogenous pressure. The voltage profile (cycling at 0.1 C, 43 μA/cm^2, 2.3 mg/cm^2) is shown in Figure 6a. During the first cycle, there is some irreversibility (Coulombic efficiency of 83 %) typical of NMC materials. The following cycles delivered almost full capacity (185.8 mAh/g) with good reversibility (Coulombic efficiency of ~99.6 % at the 2nd cycle). Afterward, the capacity gradually faded and maintained 82.4 % of capacity after 30 cycles (Figure 6b).

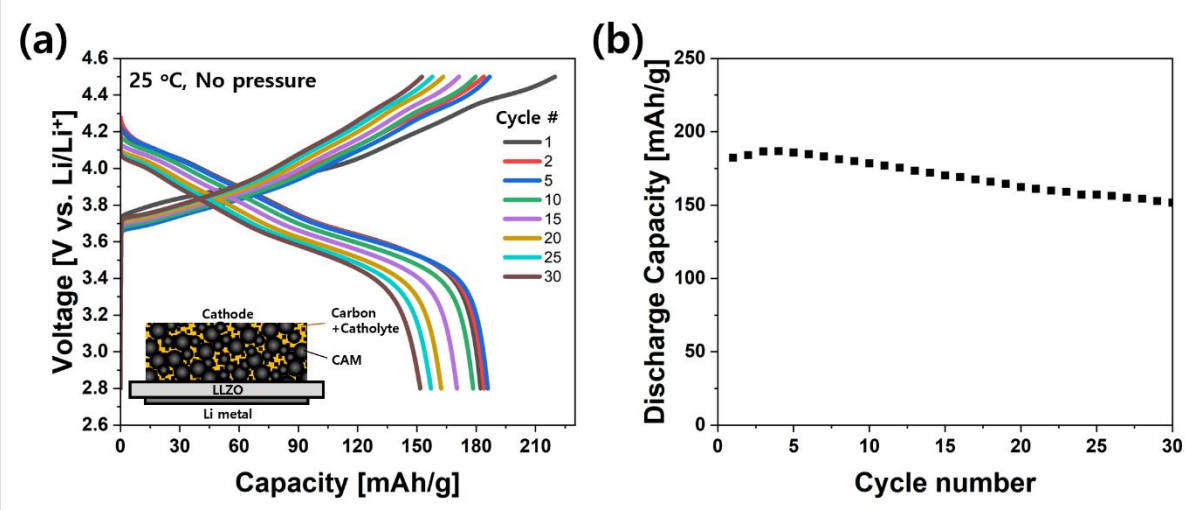

Figure 6. Li/MgO-LLZO/NMC full cell test. (a) Voltage profile and (b) cycling performance of the full cell cycled at 25 ℃, 0.1 C-rate, with no added pressure or liquid.

Conclusions

We used MgO nanopowder or fiber additives to improve the mechanical strength of thin LLZO electrolytes. The microstructures, and physical and electrochemical properties of the LLZO films processed with MgO were compared with pristine LLZO. MgO powder suppressed abnormal grain growth over long sintering times and resulted in fine and uniform grains of LLZO. SEM/EDS analysis indicated that MgO was located at grain boundaries. The mechanical strength of the LLZO films were significantly improved when MgO nanopowder (~60 %, 230 MPa) and fibers (~70 %, 261 MPa) were used, while maintaining high ionic conductivity (~$1x10^{-4}$ S/cm at room temperature). The improvement in mechanical properties is associated with a two-fold (MgO fiber) to three-fold (Mg powder) increase in the CCD compared to the pristine LLZO. A full Li/MgO-LLZO/NMC cell was assembled and cycled at room temperature, without using additional pressure or any liquid, and delivered the full expected capacity with little fading. Additional benefits to this approach are simplicity and scalability.

Acknowledgements

This work was supported by the Assistant Secretary for Energy, Efficiency and Renewable Energy, Office of Vehicle Technologies of the U.S. Department of Energy under Contract No. DE-AC02-05CH11231. We thank Jeremy Demarteau and the group of Brett Helms at LBNL for use of the DMA.

References

1. L. Xu, J. Li, W. Deng, H. Shuai, S. Li, Z. Xu, J. Li, H. Hou, H. Peng, G. Zou and X. Ji, *Advanced Energy Materials*, 2020, **11**.
2. E. Yi, H. Shen, S. Heywood, J. Alvarado, D. Y. Parkinson, G. Chen, S. W. Sofie and M. M. Doeff, *ACS Applied Energy Materials*, 2020, **3**, 170-175.
3. K. V. Kravchyk, D. T. Karabay and M. V. Kovalenko, *Sci Rep*, 2022, **12**, 1177.
4. R. A. Jonson, E. Yi, F. Shen and M. C. Tucker, *Energy & Fuels*, 2021, **35**, 8982-8990.
5. M. Rosen, R. Ye, M. Mann, S. Lobe, M. Finsterbusch, O. Guillon and D. Fattakhova-Rohlfing, *Journal of Materials Chemistry A*, 2021, **9**, 4831-4840.
6. W. Go, D. Y. Parkinson, D. Oropeza, V. Zorba, S. S. Murali, M. M. Doeff and M. C. Tucker, *ACS Energy Letters*, 2024, **9**, 2867-2875.
7. G. T. Hitz, D. W. McOwen, L. Zhang, Z. Ma, Z. Fu, Y. Wen, Y. Gong, J. Dai, T. R. Hamann, L. Hu and E. D. Wachsman, *Materials Today*, 2019, **22**, 50-57.
8. R. O. Ritchie, *Nat Mater*, 2011, **10**, 817-822.
9. M. Ruhle and A. G. Evans, *Progress in Materials Science*, 1989, **33**.
10. J. R. Kelly and I. Denry, *Dent Mater*, 2008, **24**, 289-298.
11. S. M. Wiederhorn, *Annual Review of Materials Science*, 1984, **14**, 373-403.
12. D. Sridhar, S. Purushothaman, S. Jayakumar, B. M. John, K. Chandran and H. Pulidindi, *Journal of Scientific Dentistry*, 2023, **13**, 28-30.

13. S. N. Heavens, *Journal of materials science*, 1988, **23**, 3515.
14. L. Viswanathan, Y. Ikuma and A. V. Virkar, *Journal of Materials Science*, 1983, **18**.
15. D. Olson and L. C. D. Jonghe, *Journal of Materials Science*, 1986, **21**, 6.
16. C. E. Athanasiou, M. Y. Jin, C. Ramirez, N. P. Padture and B. W. Sheldon, *Matter*, 2020, **3**, 212-229.
17. H.-Y. Li, B. Huang, Z. Huang and C.-A. Wang, *Ceramics International*, 2019, **45**, 18115-18118.
18. X. Huang, Y. Lu, Z. Song, T. Xiu, M. E. Badding and Z. Wen, *Journal of Energy Chemistry*, 2019, **39**, 8-16.
19. X. Huang, T. Xiu, M. E. Badding and Z. Wen, *Ceramics International*, 2018, **44**, 5660-5667.
20. W. Go, M. C. Tucker and M. M. Doeff, *Journal of The Electrochemical Society*, 2024, **171**, 020524.
21. R. Wagner, G. J. Redhammer, D. Rettenwander, G. Tippelt, A. Welzl, S. Taibl, J. Fleig, A. Franz, W. Lottermoser and G. Amthauer, *Chem Mater*, 2016, **28**, 5943-5951.
22. T. K. Gupta, *Journal of Materials Science*, 1971, **6**, 24-32.
23. L. Cheng, W. Chen, M. Kunz, K. Persson, N. Tamura, G. Chen and M. Doeff, *ACS Appl Mater Interfaces*, 2015, **7**, 2073-2081.
24. J. Su, X. Huang, Z. Song, T. Xiu, M. E. Badding, J. Jin and Z. Wen, *Ceramics International*, 2019, **45**, 14991-14996.
25. S. Qin, X. Zhu, Y. Jiang, M. e. Ling, Z. Hu and J. Zhu, *Applied Physics Letters*, 2018, **112**, 113901.
26. S. I. Bae and S. Baik, *Journal of the American Ceramic Society*, 1994, **77**, 2499-2504.
27. F. J. T. Lin, L. C. de Jonghe and M. N. Rahaman, *Journal of the American Ceramic Society*, 1997, **80**, 2891-2896.
28. K. A. Berry and M. P. Harmer, *Journal of the American Ceramic Society*, 1986, **69**, 143-149.
29. N. J. Shaw and R. J. Brook, *Journal of the American Ceramic Society*, 1986, **69**, 107-110.
30. X. Huang, C. Liu, Y. Lu, T. Xiu, J. Jin, M. E. Badding and Z. Wen, *Journal of Power Sources*, 2018, **382**, 190-197.
31. H. Guo, J. Su, W. Zha, T. Xiu, Z. Song, M. E. Badding, J. Jin and Z. Wen, *Journal of Alloys and Compounds*, 2021, **856,** 157222.
32. G. Han, B. Kinzer, R. Garcia-Mendez, H. Choe, J. Wolfenstine and J. Sakamoto, *Journal of the European Ceramic Society*, 2020, **40**, 1999-2006.
33. F. P. Knudsen, *Journal of the American Ceramic Society*, 2006, **42**, 376-387.
34. G. M. Song, Y. Zhou and Y. Sun, *Ceramics International*, 1999, **25**, 4.
35. N. Soga and O. L. Anderson, *Journal of the American Ceramic Society*, 1966, **49**, 355-359.
36. S. Yu, R. D. Schmidt, R. Garcia-Mendez, E. Herbert, N. J. Dudney, J. B. Wolfenstine, J. Sakamoto and D. J. Siegel, *Chemistry of Materials*, 2015, **28**, 197-206.
37. S. Yu and D. J. Siegel, *Chemistry of Materials*, 2017, **29**, 9639-9647.

Data availability

The data supporting this article have been included as part of the Electrical Supporting Information (ESI).